Review of Scientific Instruments

RESEARCH ARTICLE | MAY 08 2026

A continuous-operation sub-Kelvin scanning tunneling microscope with high magnetic field via a remote liquefaction cryogen-free scheme

Ruisong Ma ; Yuanzhi Huang ; Guangyuan Han; Hao Li ; Chenshuai Shi; Fan Wang ; Xiaodong Yu; Songping He ; Dairong Liu ; Li Liu ; Shesong Huang ; Hong-Jun Gao ; Qing Huan

Rev. Sci. Instrum. 97, 053701 (2026)
https://doi.org/10.1063/5.0325806

AIP Publishing

Review of Scientific Instruments ARTICLE pubs.aip.org/aip/rsi

A continuous-operation sub-Kelvin scanning tunneling microscope with high magnetic field via a remote liquefaction cryogen-free scheme

Cite as: Rev. Sci. Instrum. 97, 053701 (2026); doi: 10.1063/5.0325806
Submitted: 2 February 2026 • Accepted: 18 April 2026 •
Published Online: 8 May 2026

Ruisong Ma,[1,2] Yuanzhi Huang,[1,2,3] Guangyuan Han,[1,2] Hao Li,[4] Chenshuai Shi,[4] Fan Wang,[5] Xiaodong Yu,[1,2] Songping He,[1,2,3] Dairong Liu,[1,2] Li Liu,[1,2,4] Shesong Huang,[5] Hong-Jun Gao,[1,3,6] and Qing Huan[1,2,3,4,a)]

AFFILIATIONS

[1] Beijing National Center for Condensed Matter Physics and Institute of Physics, Chinese Academy of Sciences, Beijing 100190, People's Republic of China
[2] Beijing Key Laboratory of Atomic-scale Manufacturization and Advanced Vacuum System, Beijing 100190, People's Republic of China
[3] School of Physical Sciences, University of Chinese Academy of Sciences, Beijing 100190, People's Republic of China
[4] ACME (Beijing) Technology Co., Ltd., Beijing 101407, China
[5] Beijing Physike Technology Co., Ltd., Beijing 100085, China
[6] Hefei National Laboratory, 230088 Hefei, Anhui, People's Republic of China

[a)] **Author to whom correspondence should be addressed:** huanq@iphy.ac.cn

ABSTRACT

We have developed a cryogen-free ultra-low temperature scanning tunneling microscope (STM) system based on remote liquefaction technology. Integrated with a cryogen-free room-temperature bore 5 T superconducting magnet, the system achieves continuous and stable operation in the sub-Kelvin and high magnetic field regime. A two-stage ^{4}He circulation (~20 and ~2 K) precools a continuous-flow STM insert, after which another circulation loop, filled with either ^{3}He or ^{4}He, is liquefied and further cooled by evaporative pumping. The sample stage reaches base temperatures of 420 mK (^{4}He–^{3}He mode) and 894 mK (^{4}He–^{4}He mode). The temperature fluctuations of approximately ±0.1 mK are achieved at 500 mK and 1 K under proportional–integral–derivative control. Characterization, including cooling curves, current noise, thermal drift, atomic-resolution imaging, and variable-temperature/magnetic-field spectroscopy, demonstrates the performance comparable to conventional liquid-^{4}He bath-based STM systems in terms of resolution, stability, and tunability. Furthermore, the system enables a months-long continuous operation across a wide temperature range, featuring straightforward magnet upgradability, direct high-temperature baking capability, and compactness with low installation requirements. This cryogen-free design provides a viable approach for other vibration-sensitive, high-precision experiments requiring long-term continuous operation under extreme conditions.

I. INTRODUCTION

Since its invention in the 1980s,[1] scanning tunneling microscopy (STM) has become a key tool for atomic-scale imaging, spectroscopy, nanofabrication, and *in situ* characterization.[2] To meet growing research demands, STM technology continues to push toward extreme experimental conditions. Its operational temperature has progressively extended from liquid-helium (4.2 K)[3–10] to the sub-Kelvin[11–20] and even millikelvin regimes.[21–23] At these ultra-low temperatures, thermal broadening is significantly suppressed, leading to improved energy resolution and measurement stability.[3] When combined with strong magnetic fields[24] and microwaves,[25,26] cryogenic STM enables precise detection and manipulation of local electronic states. This capability provides critical experimental insights into emergent phenomena, including superconducting

mechanisms,[27,28] topological surface states,[29,30] and atomic-scale magnetic structures.[31,32]

Several research groups have developed sub-Kelvin (sub-K) high-magnetic-field STM systems, with commercial versions also available (e.g., Unisoku USM1300). Their mainstream schemes employ ^{3}He adsorption refrigeration: liquid ^{4}He in a bath cryostat is used to precool ("wet" cryogenic method) and liquefy ^{3}He (via J–T expansion or a 1 K pot), after which an adsorption pump evaporates the ^{3}He to reach base temperatures of 240–400 mK.[11–14,16–19] Because the liquid ^{3}He must be replenished after consumption, this approach is termed "single-shot" mode. Its holding time depends on the ^{3}He storage volume and the adsorption pump's capacity. An alternative "external circulation" mode employs a vacuum pump station to continuously recirculate ^{3}He, which is also precooled by liquid ^{4}He, achieving a base temperature ~400 mK.[15] This temperature is typically higher than in single-shot operation because the continuous injection of liquid ^{3}He introduces a finite steady-state heat load, whereas single-shot mode fully condenses the ^{3}He *in situ*, avoiding such parasitic heating and thereby enabling improved thermal coupling to the adsorption pump, which also resides at cryogenic temperatures.

High magnetic fields are typically supplied by superconducting magnets immersed in liquid ^{4}He. However, both ^{3}He refrigeration and "wet" magnet systems rely on finite liquid helium, which restricts continuous operation to days and necessitates periodic refilling. Varying temperature and magnetic field accelerate helium boil-off, further reduce cryogenic hold times, and restrict uninterrupted, cryogenic-to-ambient temperature sweeps. Since superconducting magnets cannot withstand the high temperatures (e.g., 150 °C) required for ultrahigh vacuum (UHV) baking, traditional wet systems necessitate physically isolating the STM insert from the cryostat, either by lifting the insert or lowering the dewar to achieve base pressures in the 10^{-10}–10^{-11} mbar range.

Global helium shortages and rising costs have accelerated the adoption of cryogen-free (closed-cycle or "dry") refrigeration across various fields, including magnetic resonance imaging (MRI),[33] quantum computing,[34] and vibration-sensitive STM.[6,8–10,35] To date, cryogen-free STM systems have achieved base temperatures near 1.4 K[35] and magnetic fields up to 12 T.[16] However, the development of a cryogen-free STM system that simultaneously operates in the sub-K regime and provides high magnetic field capability has rarely been reported.

Our team previously proposed a cryogen-free refrigeration scheme based on remote liquefaction, where a Gifford–McMahon (GM) cryocooler, housed in an independent liquefaction chamber, supplies liquid ^{4}He to the STM system.[8] The cryogen-free STM constructed via this scheme enables a months-long continuous operation below 3 K, supporting atomic-scale imaging and spectroscopic characterization. Based on this remote liquefaction architecture, this paper reports a newly developed sub-K high-magnetic-field STM system for sustained multi-month measurements. The system achieves a 420 mK base temperature, a 610 mK effective electron temperature, and a temperature stability of approximately ±0.1 mK in the sub-K regime. Compatible with room-temperature (RT) bore superconducting (SC) magnets, it was experimentally validated using a 5 T cryogen-free magnet. Owing to the modular design of the refrigeration and magnet configuration, the system allows direct high-temperature baking of UHV components without damaging the superconducting magnet or cryocooler, while allowing future integration with higher-field or vector magnets.

Experimental results demonstrate the system capabilities in imaging, spectroscopy, magnetic field modulation, and temperature-dependent characterization. Compared with conventional liquid helium-based (wet) sub-K high-magnetic-field STM systems, our cryogen-free instrument delivers comparable performance while offering distinct advantages—long-term continuous operation, wide-temperature-range regulation, flexible magnet upgradability, direct high-temperature bakeout capability, compact size, and minimal installation constraints, making it a highly competitive technological solution. Furthermore, this cryogen-free scheme provides an ideal platform for training artificial intelligence in STM operation and characterization, advancing atomic-scale manufacturing, and enabling long-term autonomous remote operation.

II. SYSTEM OVERVIEW

The developed system features four key modules: the UHV subsystem with fast entry, preparation and STM components; ^{4}He circulation; ^{3}He circulation; and magnetic field generation. It occupies a footprint of roughly 3 × 2.6 × 2.8 m^3 and is fully installed above ground. Our compact design significantly reduces infrastructural demands, allowing for simplified installation in standard-height laboratories without the need for excavation work. This section details the system design and basic operational procedures.

A. UHV subsystem

The UHV STM system consists of three independent chambers: a fast-entry load lock (LL) chamber for sample/probe exchange, a preparation chamber for sample preparation, and an analysis chamber housing the STM for imaging and scanning tunneling spectroscopy (STS) characterization [Fig. 1(a)]. Each chamber is isolated by VAT gate valves. These three chambers are supported by an aluminum profile frame. To further optimize mechanical stability, four 25 kg lead (Pb) counterweights were installed at the base corners of the aluminum frame, effectively increasing the inertial mass and suppressing low-frequency vibrations. A shared vacuum pumping unit—comprising a dry scroll backing pump (Edwards nXDS6i) and a turbomolecular pump (Edwards nEXT300D)—can be connected individually to each chamber and associated gas-handling lines (e.g., dosing lines) to provide the required high-vacuum environment. The overall pressure is monitored with a full-range gauge (Agilent FRG-730). The three-dimensional layout is illustrated in Fig. 1(b).

The LL chamber is constructed from 304 stainless steel (SS), equipped with a quick-access door and an observation viewport. After evacuation, it reaches a base pressure of ~2 × 10^{-8} mbar. A top-mounted four-slot storage dock holds probes and sample holders, which can be transferred into the preparation chamber via a magnetic transfer rod.

The preparation chamber is constructed from 304 SS and includes multiple viewports for real-time observation. It is evacuated by a sputter ion pump (SKY SIP400) and monitored with a B-A ion gauge (Agilent UHV-24), achieving a base pressure below 5 × 10^{-10} mbar after baking. A custom-built manipulator inside the chamber enables *in situ* sample processing and material growth

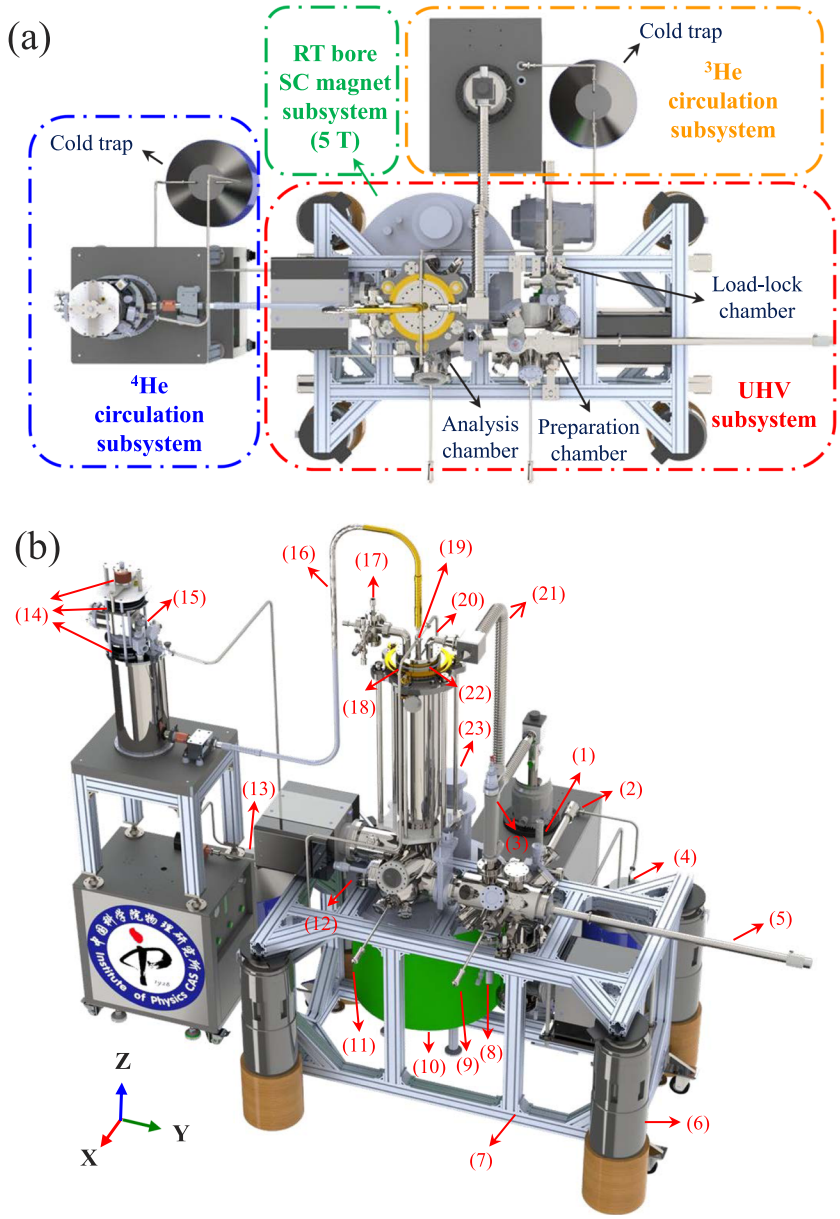

FIG. 1. 3D model of the cryogen-free, sub-K, 5-T STM system. (a) Top view of the system. It consists of four parts: ^{4}He circulation, ^{3}He circulation, RT bore SC magnet (5 T), and UHV subsystems. (b) Isometric view of the system. The marked core components are (1) load-lock dock, (2) transfer rod of load-lock chamber, (3) manipulator, (4) cold trap for ^{3}He circulation, (5) transfer rod of preparation chamber, (6) pneumatic legs, (7) aluminum profile support, (8) ion source, (9) wobble stick of preparation chamber, (10) RT bore SC magnet, (11) wobble stick and (12) dock of analysis chamber, (13) cold trap for ^{4}He circulation. (14) SS bellows suspension, (15) GM cryocooler, (16) liquid ^{4}He transfer line, (17) DN40CF six-way cross with feedthroughs, (18) ^{4}He gas return line, (19) ^{4}He inlet, (20) ^{3}He inlet, (21) ^{3}He gas return line, (22) 600-mm linear actuator, and (23) pulse tube (PT) cryocooler.

via resistive heating (ACME MTC110 controller) and electron-beam bombardment (ACME EBC200 controller). An Ar^+ ion source (Prevac IS-40) is aligned with the sample stage for surface cleaning or ion etching. Samples and probes are held in place by a magnetic transfer rod with an eight-slot dock, and a wobble stick assists in transferring holders between the manipulator and the storage dock.

The upper portion of the analysis chamber, also made of 304 SS, is pumped by a sputter ion pump (SKY SIP400) and monitored with a B-A ion gauge (Agilent UHV-24), maintaining a vacuum of below 5×10^{-10} mbar. Inside the analysis chamber, a five-slot storage dock accommodates samples and probes. These are transferred from the preparation chamber via a magnetic transfer rod through an open gate valve and are positioned using a wobble stick. A DN160CF heavy-duty linear actuator (load capacity ≈ 50 kg), mounted atop the chamber, drives the STM insert vertically [Fig. 2(a)]. The lower section consists of a cylindrical 316L-SS cavity, concentrically aligned with the STM insert and the RT bore SC magnet. The linear actuator offers 600 mm of travel. In the raised state, the wobble stick allows the probe and sample exchange on the scanner [Fig. 2(b)]. After being lowered by 530 mm, the scanner is positioned fully within the 316L-SS cavity, aligning the STM probe and sample with the magnetic-field center [Fig. 2(c)].

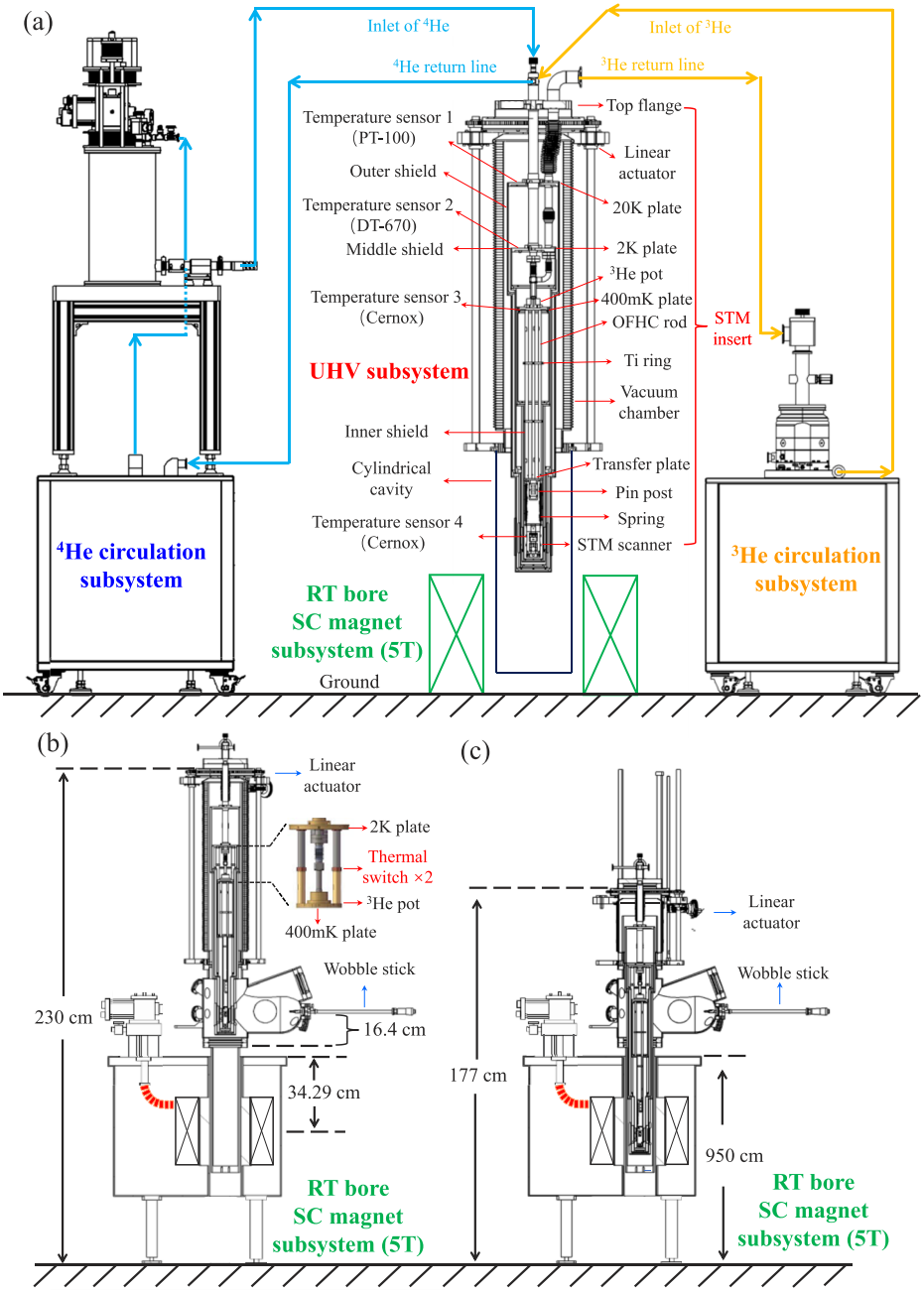

FIG. 2. Schematic diagram of the system working principle. (a) Schematic diagram of the core composition of the system. The ^{4}He circulation subsystem precools 20 and 2 K plates of the STM insert and the ^{3}He circulation loop. The pre-cooled and liquefied ^{3}He in the ^{3}He pot is subsequently evaporated to cool the 400 mK plate. The RT bore SC magnet provides a high magnetic field environment for the STM. Cross-sectional schematic diagram of the scanner in the probe/sample replacement position (b) and in the magnetic field center position (c). The two identical thermal switches are highlighted in (b).

B. STM insert and system control

The STM insert, the core of the system, is assembled from top to bottom as follows [Fig. 2(a)]: a top flange, a 20 K plate, a 2 K plate, a ^{3}He pot, a 400 mK plate (mounted directly below the ^{3}He pot), three thermally conductive oxygen-free high-conductivity (OFHC) copper support rods, two titanium rings, an electrode-transfer plate, a spring assembly, and the STM scanner. The top flange contains inlet/outlet ports for ^{3}He and ^{4}He and serves as the feedthrough interface for all electrical signals. To ensure precise positioning of the STM scanner at the magnetic field center and efficient thermal conduction from the 400 mK plate to the bottom-mounted scanner, three thermally conductive OFHC rods (8 mm in diameter, 450 mm in length) are installed beneath the 400 mK plate. The bottom ends of the OFHC rods are connected to a lower OFHC transfer plate for electrodes, and the middle parts of the rods are secured by two titanium rings, enhancing the structural rigidity [Fig. 2(a)]. Since the entire elongated STM insert is over 1 m in length, special attention

must be paid to alignment during installation to prevent contact between the magnet, 316L-SS cavity, three-layer shields, and the scanner, thereby avoiding mechanical contact and thermal shorts. For specific details about alignment of these components, please refer to the supplementary material.

To facilitate rapid cooling, two identical adsorption-type gas-gap thermal switches are integrated between the 2 K plate and the 400 mK plate [Fig. 2(b)], which automatically decouples the two plates at ~15 K. The component features a composite tube comprising an SS upper section and a copper lower section. This housing encloses two copper leads at its ends, while the internal volume is filled with a small amount of ^{4}He gas and activated charcoal. At temperatures exceeding ~15 K, internally sealed ^{4}He gas provides a high-conductance path between the 2 K plate and the 400 mK plate. Below this threshold, activated charcoal within the switch adsorbs the ^{4}He gas, resulting in a vacuum gap that thermally isolates the two plates, enabling the ^{3}He pot to reach its base temperature independently.

To suppress radiative heat loads, the insert employs a triple-layer radiation shield configuration. The outer, middle, and inner shields are thermally anchored to the 20, 2 K, and 400 mK plates, respectively (all stages are gold-plated OFHC). The outer and middle shields are fabricated from 1-mm-thick 6061 aluminum alloy and attached to the 20 and 2 K plates using titanium screws, balancing thermal conductivity and radiative isolation. To improve thermal coupling, soft copper braids (~2 mm in diameter) are added between the base at the bottom and the atop OFHC plate for the outer and middle shields. To prevent mechanical contact or thermal shorts between the closely spaced shields, these braids are constrained and secured tightly against the shield surfaces using 0.5-mm copper wires, maintaining necessary radial clearances throughout the meter-long assembly. The inner shield is made of 1-mm-thick OFHC with a diameter of 75 mm. Each of the triple-layer shields is fitted with an independent, horizontally actuated door, operated sequentially via the wobble stick in the analysis chamber to allow probe and sample exchange [Fig. 2(b)]. Furthermore, two braids with a diameter of ~1 mm are installed between each door and its corresponding shield base to ensure thermal equilibrium and minimize the heat load.

The STM scanner used in this system follows a modified Pan-type scanner design, with a diameter of ~35 mm and a height of ~88 mm.[4,8] In contrast to earlier customized scanners, the present version is constructed entirely from non-magnetic materials. It is suspended by three beryllium-copper springs (wire diameter 0.4 mm, outer diameter 5.3 mm) and connected to the electrode transfer plate via two orthogonally arranged sets of C-shaped copper braids (not shown), which provide both thermal conduction and mechanical damping. Additional vibration isolation from the ground is achieved through four pneumatic leg springs (Newport S-2000A) supporting the aluminum-profile frame of the UHV subsystem [Fig. 1(b)].

Four temperature sensors are mounted inside the STM insert: a PT-100 platinum resistance thermometer (minimum 20 K) on the 20 K plate; a DT-670 silicon diode thermometer (minimum 1.4 K) on the 2 K plate; and two Cernox thermometers (minimum 250 mK) on the 400 mK plate and the scanner sample stage [Fig. 2(a)]. In addition, each of the 20 and 2 K plates is equipped with a metal-ceramic heater (MCH, 30 Ω), while the 400 mK plate and the scanner stage each carry a 50 Ω thin-film chip resistor, enabling precise temperature control during variable-temperature measurements.

To minimize heat conduction, the signal wiring employs a single-stage electrode transfer and multiple thermal-anchoring stages. Between the scanner and the transfer plate [Fig. 2(a)], coarse positioning, scanning control, heater, and temperature sensor signals are carried by soft copper wires, while the tunneling current (I_t) and bias voltage (V_{bias}) lines use silver-alloy coaxial cables. The electrode pin post on the transfer plate is made of aluminum nitride and contains an array of 0.6 mm-diameter holes through which 0.5 mm beryllium-copper wires are threaded and secured with epoxy (EPO-TEK H74F). Silver-alloy coaxial cables are thermally anchored to the OFHC transfer plate via SSMA adapters to reduce crosstalk.

From the transfer plate to the top flange, coarse positioning, scanning control, heater, and temperature sensor signals are routed using manganin twisted-pair wires, whereas I_t and V_{bias} lines are implemented with SS coaxial cables to further limit thermal leakage. All wiring is wound around a central SS tube, wrapped in PTFE tape, and thermally anchored at the 2 and 20 K plates.

All electrical feedthroughs are grouped on a six-way cross mounted atop the DN160CF flange [Fig. 1(b)]. The STM is controlled by a high-precision electronic suite consisting of a commercial current preamplifier (Femto DLPCA-200) and an STM controller with a lock-in module (Nanonis, SPECS GmbH). To suppress radio frequency noise and improve energy resolution in STS measurements, homemade copper-powder filters, RC filters, and π-filters were installed on the feedthroughs (for more details, refer to Fig. S1 in the supplementary material), and an attenuator (1×, 10×, 100× selectable) was integrated into the V_{bias} line. Temperature sensors are monitored and regulated by a Cryo-con 24C unit, with data logging and analysis performed via custom-written software.

C. Operation of refrigeration and magnet subsystems

The cryogen-free system attains cryogenic and high-magnetic-field conditions via three subsystems: ^{4}He circulation, ^{3}He circulation, and the RT bore SC magnet subsystems [Fig. 2(a)]. The ^{4}He circulation loop precools the 20 and 2 K plates of the STM insert and the ^{3}He circulation loop. The cold traps for purifying ^{4}He and ^{3}He gas are immersed in a 50 L LN_2 dewar (Fig. 1) with a two-week hold time, and routine LN_2 refilling does not interrupt STM operations. After precooling and liquefaction, the liquid ^{3}He is stored in the ^{3}He pot and subsequently evaporated to cool the 400 mK plate by the circulating pumps. The SC magnet is cooled independently by a pulse-tube (PT) cryocooler. Cooling water for the GM cryocooler (Sumitomo RDE-418E4), helium compressor-1 (Sumitomo F-50), PT cryocooler (Sumitomo RP-082B2S), and helium compressor-2 (Sumitomo F-70) is supplied by an air-cooled chiller (Kyushu Honest FT-14DP). The full circulation scheme is shown in Fig. 3, and the main steps to reach cryogenic temperatures and high magnetic fields are outlined below.

1. The ^{4}He circulation is initiated by evacuating the gas circuit (valves V1–V5 open) to ~10^{-6} mbar using a mobile vacuum pump connected to V1. After closing V1, about 10 L of ^{4}He gas is charged through V6. A liquid-nitrogen cold trap (trap-1) purifies the circulating ^{4}He to prevent impurity-induced blockages. Pressure is balanced by a ^{4}He gas bellows tank, maintaining the circuit near 1 atmospheric pressure. Upon

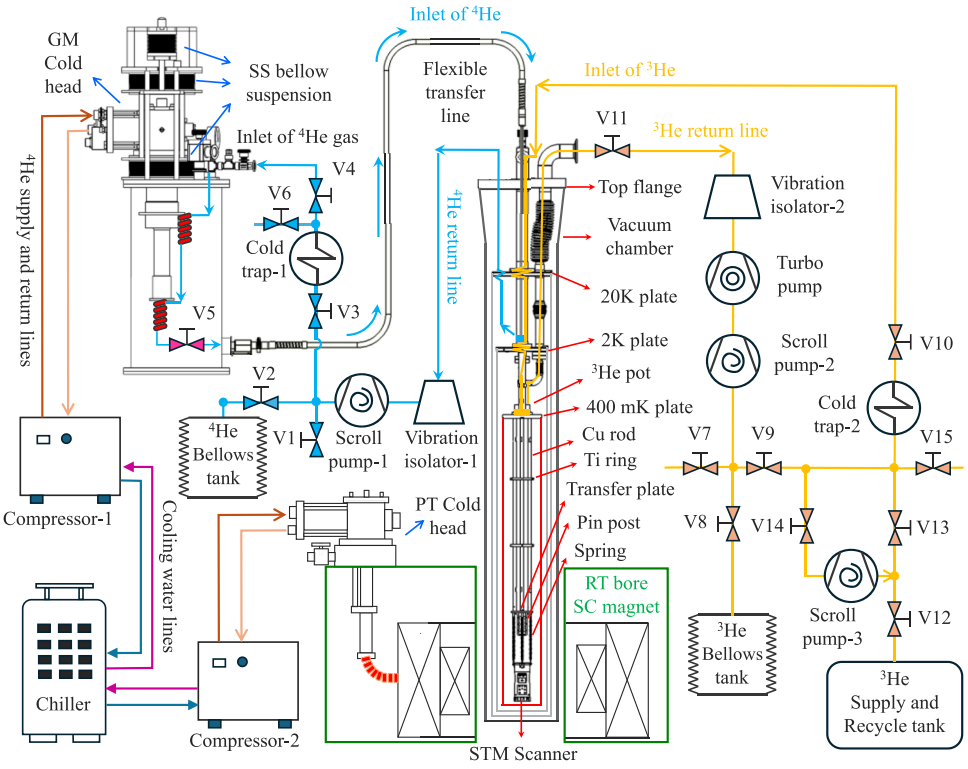

FIG. 3. Schematic diagram showing the circulation of the cryogen-free STM system. The system consists of three refrigeration subsystems: ^{4}He circulation, ^{3}He circulation, and RT bore SC magnet subsystems. The sub-K temperature regime is achievable by filling the ^{3}He circulation with either ^{3}He (^{4}He–^{3}He mode) or ^{4}He (^{4}He–^{4}He mode). The RT bore SC magnet is cooled by an independent pulse tube (PT) cryocooler.

starting the GM cryocooler and dry-scroll pump-1 (Edwards nXDS15iR), the ^{4}He gas circulates, exchanging heat with the two-stage cold head of the GM cryocooler. After ~20 h, liquid ^{4}He forms and can be throttled through needle valve V5 into the superfluid state (<2.17 K). Mechanical vibration from the GM cryocooler is attenuated via three-stage welded 304 SS bellows. Superfluid ^{4}He is delivered via a flexible transfer line to cool the 2 K plate, from which vaporized gas is used to cool the 20 K plate. With only the ^{4}He subsystem running, the scanner sample stage reaches a minimum achievable temperature of ~2.5 K. The return gas line is vibration-isolated by a mass-loaded SS block (isolator-1). For ^{4}He recovery, valve V3 is closed and V2 opened, returning the gas to the bellows tank. To regenerate cold trap-1 after the ^{4}He gas recovery, valves V3 and V5 are closed and the trap is warmed to room temperature; impurity gases are then evacuated via V6 using a vacuum pump. The ^{4}He circulation subsystem design is based on our earlier work on sub-3 K equipment.[8]

2. The ^{3}He circulation subsystem is initiated by evacuating the gas circuit (valves V7–V11 open) to ~10^{-5} mbar using a vacuum pump connected to V7. After closing V7, valves V12 and V13 are opened to charge ~6 L of ^{3}He gas from the ^{3}He supply and recycle tank into the circuit (^{4}He–^{3}He mode) before initiating the ^{4}He circulation. The gas is purified by liquid-nitrogen cold-trap-2, after which V12 and V13 are closed. The ^{3}He is then liquefied via two-stage heat exchange with the 20 and 2 K plates followed by throttling and is collected in the ^{3}He pot. Once the ^{4}He circuit cools the 2 K plate below 3 K, the pre-charged ^{3}He has been liquefied into the ^{3}He pot. At this stage, starting dry-scroll pump-2 (Edwards nXDS15iR) and the turbomolecular pump (Edwards nEXT730D) initiates evaporative cooling of the liquid ^{3}He, lowering the 400 mK plate below 420 mK (^{4}He–^{3}He mode). The returning ^{3}He vapor provides additional cooling to the 2 and 20 K plates, as shown in Fig. 3. After exiting the top flange, the return line is vibration-isolated with sand-filled bags (isolator-2). A 304 SS bellows tank in the circuit serves only as a pressure buffer. For ^{3}He recovery, V10 is closed, while V14 is opened, and dry-scroll pump-3 (Edwards nXDS20iR) is started to return the gas to the supply and recycle tank (bottom-right of Fig. 3). To regenerate cold trap-2 after the ^{3}He gas recovery, V9 and V10 are closed, the trap is warmed to room temperature, and impurities are evacuated through V15 using a vacuum pump. The circuit can alternatively be charged with 6 L of ^{4}He gas (^{4}He–^{4}He mode), following the same operational procedure.

3. The system incorporates a cryogen-free RT bore SC magnet (Cryomagnetics, 5 T, 6-inch bore) independently cooled by a PT cryocooler and supported on four ground-mounted columns [Figs. 2(b) and 2(c)]. The STM analysis chamber's cylindrical cavity is aligned concentrically within the magnet bore while remaining mechanically isolated. The magnetic-field center lies 342.9 mm below the upper surface of the magnet bore [Fig. 2(b)]. After sample or probe exchange, a linear actuator lowers the STM insert by 530 mm, positioning the scanner at the field center [Fig. 2(c)]. Magnetic fields

are applied via a separate magnet controller (Cryomagnetics 4G-100). A current of 80 A produces a field of 5 T. To limit temperature drifts during ramping, the current sweep rate is set to 45.3 mA s^{-1} from 0 to 50 A and 22.7 mA s^{-1} from 50 to 80 A. The magnet design also allows simplified replacement with other superconducting magnets of the same or larger bore size, thereby enabling upgrades to higher fields or vector-field magnet configurations.

III. PERFORMANCE

To demonstrate the performance of our cryogen-free STM system, we carried out cooling-down tests, current spectral density (CSD) measurements of the tunneling current vs frequency, and imaging and tunneling spectroscopy measurements with temperature and magnetic field modulations.

A. Refrigeration performance

The STM insert is cooled via two independent gas circulations: ^{4}He loop and ^{3}He loop. To reduce operating costs, the ^{3}He circuit can also be charged with ^{4}He (^{4}He–^{4}He mode), which still allows sub-K cooling. In ^{4}He–^{4}He mode, the scanner stage cools from room temperature to ~2 K in about 25.8 h and reaches a base temperature of 894 mK after 35 h [Fig. 4(a)]. At this stabilized state, the temperature difference between the sample stage and the ^{3}He pot remains below 5 mK. The 20 and 2 K plates stabilize near 28 and 2.7 K, respectively, providing a low-thermal-background environment for the inner shield and scanner. When the ^{3}He pot cools below ~15 K, the gas-filled thermal switches open, decoupling the ^{3}He pot from the 2 K stage and markedly accelerating the cooling of the pot, as shown in Fig. 4(a). In ^{4}He–^{4}He mode, the natural fluctuation of the base temperature is within ±1 mK, as shown in Fig. S2(a) of the supplementary material. Closed-loop proportional–integral–derivative (PID) control via the sample-stage thin-film chip resistor maintains a long-term stability of ~±0.1 mK at 1 K over 24 h [Figs. 4(c) and 4(e)].

In ^{4}He–^{3}He mode, the scanner sample stage reaches the sub-K range in ~25 h and attains a base temperature of 420 mK after 35 h [Fig. 4(b)]. Here, the 2 K plate stabilizes around 2.5 K, while the 20 K stage falls below the lower detection limit of the Pt-100 thermometer (<20 K). As shown in Fig. S2(b) of the supplementary material, the natural fluctuation of the base temperature is within ±0.5 mK in ^{4}He–^{3}He mode. With PID control of heating with thin-film chip resistor on the scanner, the scanner sample stage maintains ~±0.1 mK stability at 500 mK over 24 h [Figs. 4(d) and 4(f)]. Provided that the circulation lines are properly sealed and pre-evacuated (e.g., with KF flanges), the system routinely achieves a sub-450 mK base temperature for over three months. A trap blockage is signaled if the 2 K plate temperature exceeds 3 K or the ^{3}He pot exceeds 500 mK with heater off, which would require a pause for regeneration. Apart from these triggers, the regeneration process is rarely needed.

Upon opening the three-layer thermal-shield doors and inserting a room-temperature sample into the scanner, the sample stage temperature rises to ~95 K and the ^{3}He pot temperature to ~18 K [Fig. 4(g)]. After reclosing the shields, both temperatures return to the sub-Kelvin range within about 1.5 h. For temperature ramping below 15 K, regulation can be performed independently via the thin-film chip resistor on the scanner sample stage, achieving a stability of ~±1 mK within several minutes [inset of Fig. 4(h)]. For higher temperatures up to 300 K, stable control can also be achieved using both thin-film chip resistors under properly tuned PID parameters, as illustrated in Fig. 4(h). Throughout the temperature ramping process, both the ^{3}He and ^{4}He circulation loops remain in normal operation without any manual adjustments or interruptions to the cooling cycle.

The cryogen-free SC magnet is cooled independently by a PT cryocooler. Its coil cools from RT to a base of ~3.3 K in ~22 h. To keep the magnet below 3.8 K, the field sweep rate is limited: ramping from 0 to 5 T takes about 34 min. Eddy currents during ramping transiently raise the sample temperature by ~0.3 K; after ~4 min, the sample re-stabilizes with a residual offset of <50 mK relative to the zero-field condition.

B. CSD measurement

To assess junction stability, we measured the CSD of the tunneling current under zero field and at 5 T, which directly reflects the mechanical and electrical stability of the probe-sample junction.

Figure 5(a) shows CSD curves up to 1 kHz for a Cu(111) surface at zero field, with the probe in three states: withdrawn, tunneling with feedback on, and tunneling with feedback off. With the probe withdrawn, the background noise remains below 20 fA $Hz^{-1/2}$ across the measured band. In the tunneling state with feedback on, the overall CSD increases due to the tunneling signal but stays below 200 fA $Hz^{-1/2}$ at its highest peak. With feedback off, sensitivity to probe-sample perturbations elevates the CSD further, especially at low frequencies; nonetheless, the noise remains under 2 pA $Hz^{-1/2}$, confirming excellent low-noise performance. The prominent peak observed at ~9 Hz is identified as a structural resonance of the slender STM insert support, which mainly consists of three 450-mm-long copper rods and a 550-mm-long ^{3}He cryostat (Fig. S4 of the supplementary material). In contrast, the prominent features above 50 Hz are attributed to gas flow fluctuations and mechanical vibrations from the circulation and turbomolecular pumps. A comprehensive analysis of these noise sources is provided in Figs. S3 and S4 of the supplementary material.

It is well known that the shorter dimensions of the supporting structure from the top flange to the transfer plate holding the scanner not only increase the rigidity of the system but also improve the cooling power. Given that the length of the ^{3}He cryostat is fixed at 550 mm, the lengths of the OFHC copper rods (450 mm) and the linear actuator (600 mm) are necessitated by the 530 mm travel range between the sample transfer position and the magnetic field center. This span is constrained by the current instrument geometry: the transfer level (i.e., the sample transfer plane where the wobble stick is located) in the raised state is 164 mm above the 316L-SS cavity's mounting flange, while the magnetic center is 342.9 mm below the magnet's top surface. These dimensions of the copper rods and linear actuator ensure that the scanner can traverse the full distance required for both sample exchange and measurement under magnetic field. Future optimizations, such as strengthening the ^{3}He cryostat, shortening the OFHC copper rods, compacting the chamber height, and reducing the magnet's field-center depth, will aim to

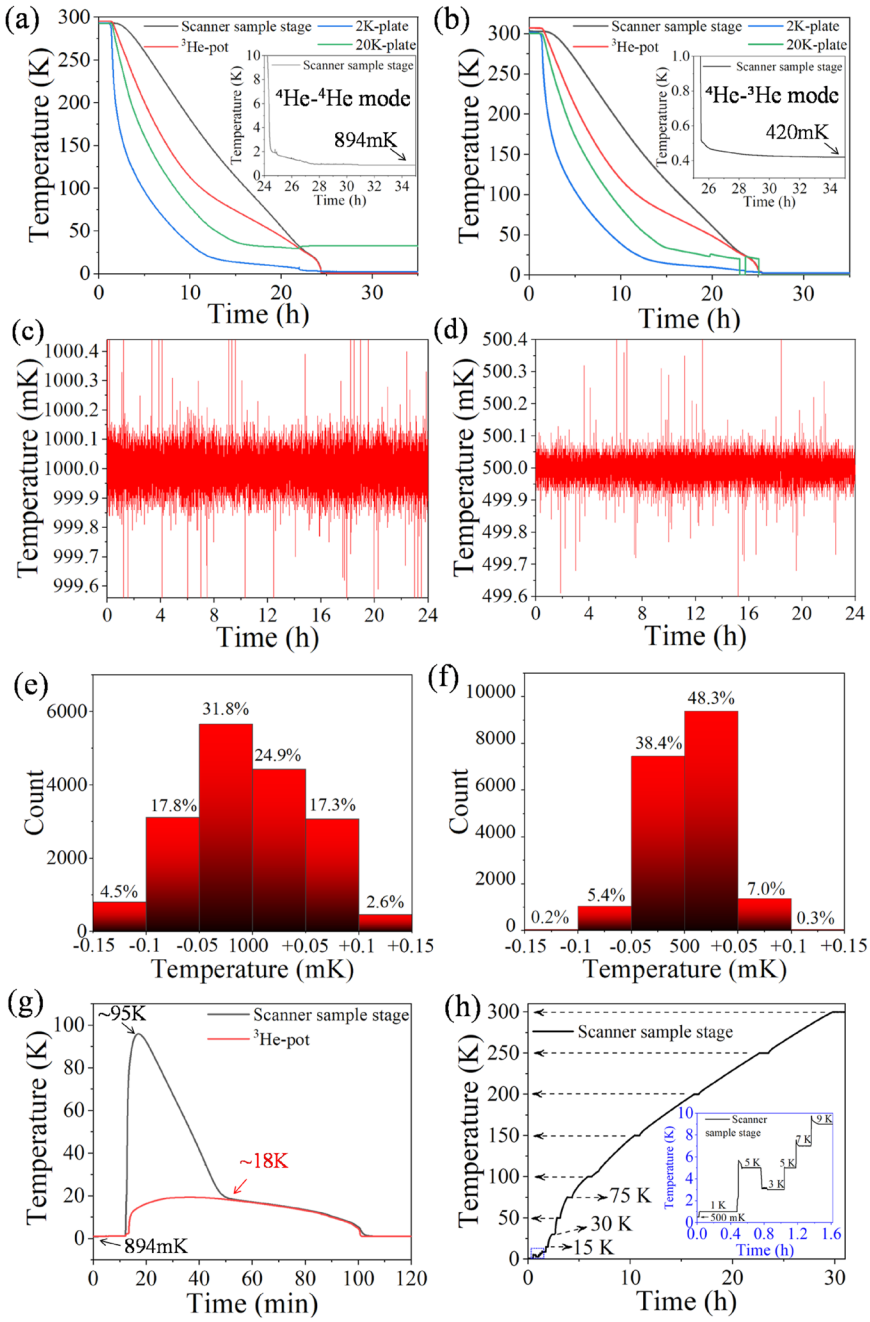

FIG. 4. Cooling performance and temperature stability of the STM system. (a) Temperature cooling curve in the ^{4}He–^{4}He mode: the scanner-sample stage requires ~25 h to cool from room temperature to the 2 K regime and reaches a base temperature of 894 mK after 35 h. (b) Temperature cooling curve in the ^{4}He–^{3}He mode: the scanner-sample stage takes ~25.8 h to cool from room temperature to the sub-Kelvin (sub-K) region, with a base temperature of 420 mK achieved at 35 h. [(c) and (d)] Temperature fluctuation profiles after thermal equilibration at 1 K and 500 mK, respectively, within a 24-h period under PID regulation. [(e) and (f)] Temperature distribution histograms of the sample stage at 1 K and 500 mK. About 91.8% (98.9%) and 99.1% (99.6%) of the measured temperatures fall within the ±0.1 mK (±0.15 mK) fluctuation range at 1 K and 500 mK, respectively. (g) Temperature variation curve following room-temperature sample replacement: the temperature difference between the ^{3}He pot and sample stage decreases to <1 K within ~40 min, and both components recover to the sub-K regime in ~1.5 h. (h) Temperature ramp curve from 500 mK to 300 K. Each plateau corresponds to a set-point temperature. The inset shows the temperature ramping between 500 mK and 9 K, corresponding to the region marked by the blue dashed box in (h).

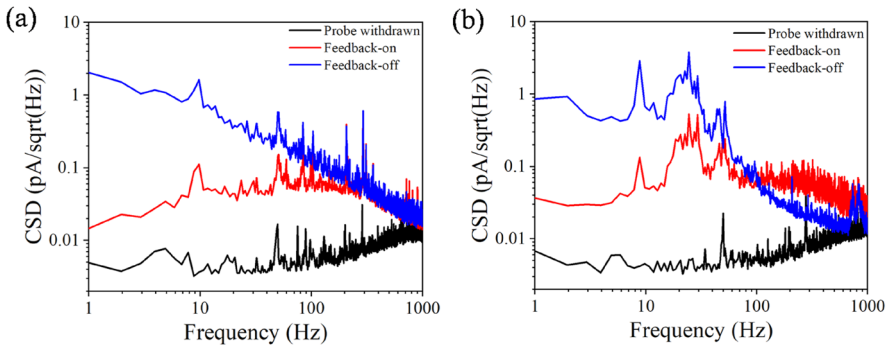

FIG. 5. Noise Spectrum at base temperature characterized by CSD at zero field and 5 T magnetic field (a) CSD of the tunneling current at 0 T; (b) CSD of the tunneling current at 5 T. Tunneling conditions in ^{4}He–^{3}He mode: [I_t = 100 pA, V_{bias} = −100 mV, sample Cu(111) @420 mK].

enhance thermal conductance and mechanical rigidity—the latter of which is expected to effectively eliminate low-frequency noise.

Under a 5 T field [Fig. 5(b)], the withdrawn-probe noise baseline (1–20 fA Hz$^{-1/2}$) matches the zero-field level. With feedback on, the overall noise is slightly higher, showing a broad feature between 15 and 35 Hz; the CSD stays below 300 fA Hz$^{-1/2}$ except for two isolated peaks near 500 fA Hz$^{-1/2}$. With feedback off, the noise reaches up to 3 pA Hz$^{-1/2}$. The elevated noise under field is attributed to vibration coupling from the PT cryocooler and ground, transmitted through the magnetic field to the tunneling current.[36]

C. STM and STS performance

The STM and STS performance of our cryogen-free system was evaluated on Cu(111), highly oriented pyrolytic graphite (HOPG), and Pb substrates.

The Cu(111) crystal (MaTecK) was prepared by repeated Ar^+ sputtering and annealing at 400 °C in the preparation chamber. Tungsten probes were fabricated by chemically etching 0.5-mm-diameter wires, followed by outgassing via thermal field emission. Before measurement, each probe was conditioned on Cu(111) using voltage pulses and controlled indentations to improve imaging and spectroscopic quality.

Figure 6(a) shows an STM image of Cu(111) at 420 mK. The strip-like features correspond to indentation structures ~210 pm deep, matching the monatomic step height of Cu(111). STS spectra acquired on the same surface reveal a pronounced surface state near 400 mV [inset of Fig. 6(b)].[37]

The minimum tunneling current reflects both instrumental and electronic noise. Figures 6(a)–6(f) present STM images of Cu(111) taken with a sample bias of −1 V and tunneling currents set to 50, 20, 10, 5, 3, and 2 pA, respectively (preamplifier gain 10^9 V A^{-1}). Image resolution gradually degrades as the current is lowered, and stable tunneling could not be maintained below 2 pA, which represents the minimum scanning current for this system.

To assess thermal stability, the scanner thermal drift was measured at 420 mK by continuously scanning a fixed area on Cu(111) for 24 h (I_t = 100 pA, V_{bias} = −100 mV). The average lateral and vertical drifts were ~30 pm h^{-1} and ~10 pm h^{-1}, respectively.

Magnetic-field tunability was tested on freshly cleaved HOPG. Figure 7(a) compares STS spectra at 0 and 5 T under different tunneling currents. At 0 T, a V-shaped spectrum is observed, whereas

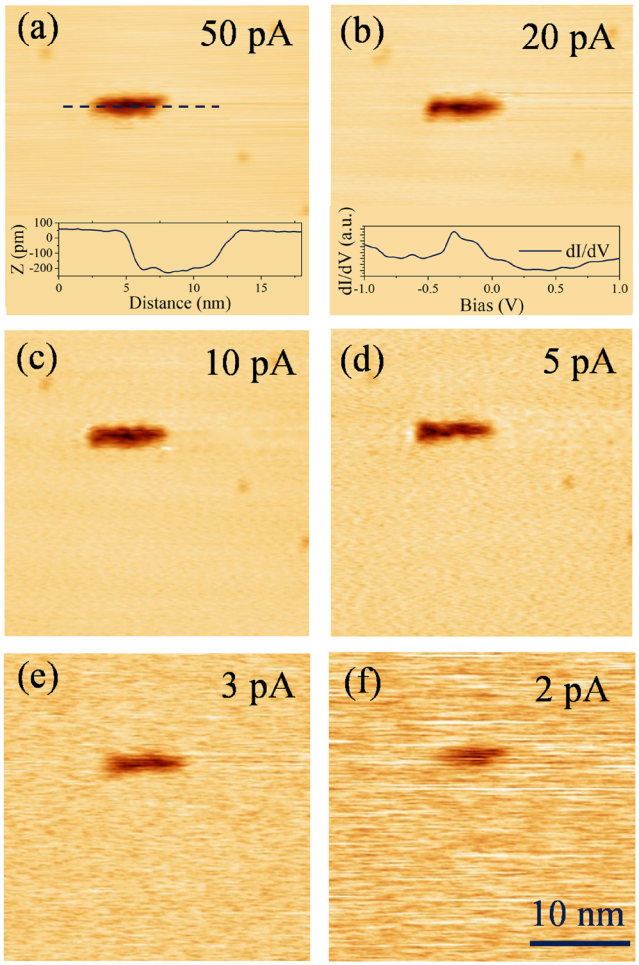

FIG. 6. Measurement of the minimum imaging tunneling current. STM images of Cu(111) were acquired at a bias voltage of −1 V with the tunneling current set to 50 pA (a), 20 pA (b), 10 pA (c), 5 pA (d), 3 pA (e), and 2 pA (f), respectively. All images have a size of 35 × 35 nm^2, with the specific scale bar provided in panel (f). (a) line profile along the hole corresponding to the dashed line shown in the image. (b) dI/dV curve measured on the Cu(111) surface. (I_t = 1 nA, V_{bias} = −1 V, bias modulation was set as 7 mVrms @973 Hz).

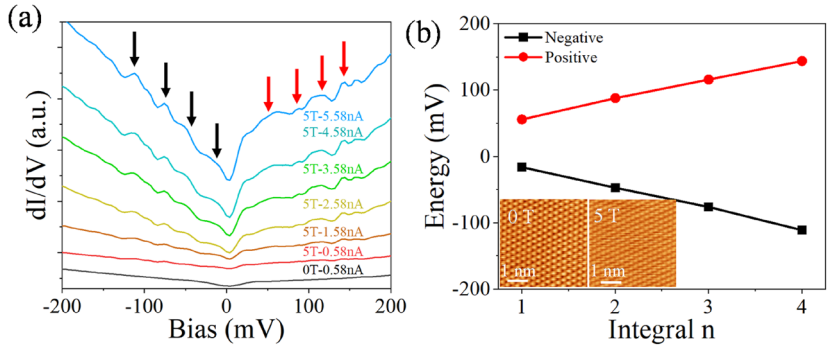

FIG. 7. Characterization of HOPG at 5 T magnetic field. (a) dI/dV spectra of HOPG taken at 5 T and 1.2 K showing Landau levels marked by arrows. The spectrum at 0 T is also shown for comparison. The current setpoint varies from 0.58 to 5.58 nA (V_{bias} = −200 mV, bias modulation was set as 5 mVrms @973 Hz). The curves are offset vertically for clarity. (b) Relationship between the integral and the Landau levels. The energy levels on negative and positive sides are both proportional to the integrals n of the level. Insets of (b) show atomic-resolution STM images of HOPG at 0 T (I_t = 100 pA and V_{bias} = −200 mV) and 5 T (I_t = 2 nA and V_{bias} = −150 mV).

Landau levels emerge clearly at 5 T. As shown in Fig. 7(b), the Landau-level signal intensifies with increasing tunneling current and follows the expected relation $E \propto n\hbar\omega_t$, consistent with earlier reports.[6,16,38] Despite higher noise under magnetic field, atomically resolved STM images of HOPG were still obtained [inset of Fig. 7(b)].

High-resolution spectroscopy was performed on a single-crystal Pb(110) (MaTecK). After repeated Ar^+ bombardment and annealing at 250 °C, the sample was transferred into the STM scanner. At base temperature, a clean Pb(110) surface was obtained [Fig. 8(a)]. Following tip conditioning, atomically resolved images were acquired [Fig. 8(b)]. The line-profile analysis of atomic corrugations indicates a vertical (Z-direction) noise floor of ~1 pm [inset of Fig. 8(b)], comparable to that of mainstream liquid-helium-based sub-K STM systems.

The high-resolution spectroscopy of the superconducting Pb(110) was performed in both refrigeration modes. In ^{4}He–^{4}He mode, fitting the tunneling spectrum with the Maki equation gives an effective electron temperature of ~1.06 K and superconducting gap of ~1.39 meV at the base temperature of 894 mK [Fig. 8(c)]. In ^{4}He–^{3}He mode with the base temperature of 420 mK, the measured spectrum corresponds to an effective electron temperature of ~610 mK and a superconducting gap of ~1.35 meV [Fig. 8(d)].[23,39] We also acquired superconducting spectra under PID temperature control. In ^{4}He–^{4}He mode, with the temperature controlled at 1 K, the fitted effective electron temperature and superconducting gap are 1.15 K and 1.39 meV, respectively [Fig. 8(e)]. In ^{4}He–^{3}He mode, with the temperature controlled at 500 mK, the fitted effective electron temperature and superconducting gap are 690 mK and 1.39 meV, respectively [Fig. 8(f)]. The superconducting gaps obtained at different temperatures are in good agreement with the reported superconducting gap of 1.36 meV for Pb(110) single crystals.[40]

Spectroscopic characterizations under varying temperatures and magnetic fields were conducted on the Pb(110) substrate. As illustrated in Figs. 8(a) and 8(b), the temperature and magnetic field dependence of the superconducting energy gap is clearly resolved. Our results indicate a superconducting transition temperature (T_c)

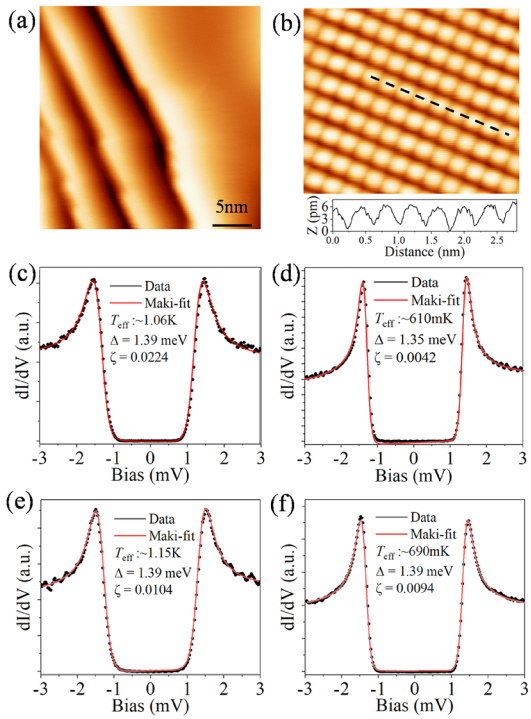

FIG. 8. Imaging and spectroscopy characterization on Pb(110) substrate. (a) Large-scale STM image of Pb(110) (I_t = 60 pA, V_{bias} = −1 V). (b) Atomic-resolution image of the Pb(110) surface (I_t = 1.81 nA, V_{bias} = 74 mV). The inset at the bottom shows the atomic line profile corresponding to the dashed line in the image, with a Z noise level of ~1 pm. The dI/dV spectra were recorded at base temperatures of 894 mK (c) and 420 mK (d), and at elevated temperatures of 1 K (e) and 500 mK (f) maintained via PID control. The solid lines represent fits using the Maki equation, with extracted parameters (effective electron temperature T_{eff}, superconducting gap Δ, depairing parameter ζ) as follows: (1.06 K, 1.39 meV, 0.0224) for (c); (610 mK, 1.35 meV, 0.0042) for (d); (1.15 K, 1.39 meV, 0.0104) for (e); and (690 mK, 1.39 meV, 0.0094) for (f). Tunneling conditions for [(c)–(f)]: I_t = 1 nA, V_{bias} = −3 mV, with a 30 μVrms bias modulation at frequencies of 579, 663, 547, and 851 Hz, respectively.

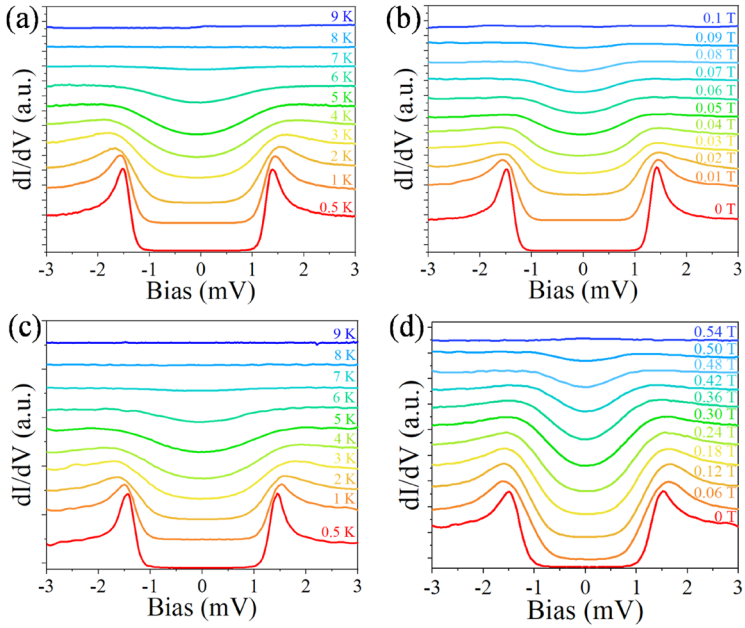

FIG. 9. Variation of the superconducting gap of Pb(110) substrate and Pb foil modulated by different temperatures and magnetic fields. Evolution of the dI/dV spectra on the Pb(110) single crystal substrate (a) and Pb foil (c) with increased sample temperature. Evolution of the dI/dV spectra of the Pb(110) single crystal (b) substrate and Pb foil (d) with ramped magnetic field at 420 mK. The curves are offset vertically for clarity (I_t = 1 nA, V_{bias} = −3 mV, bias modulation was set as 30 μVrms @973 Hz).

of ~7 K, which is in good agreement with the literature value of 7.2 K.[41] Furthermore, magnetic field-dependent measurements reveal that the superconductivity is suppressed at 0.09 T, closely matching the reported bulk critical field of 0.08 T.[41]

We also used low-cost Pb foil to test temperature and magnetic-field tunability. Before loading into the LL chamber, the surface oxide of the Pb foil was scraped off with a scalpel and the foil was quickly evacuated. The photographs of the scraped Pb foil are shown in Fig. S5 of the supplementary material. It remains stable in the atmosphere for at least 30 min and can be directly loaded into the scanner for spectroscopic characterization. Alternatively, to further remove surface oxides and impurities, the foil can undergo the same argon-ion sputtering and annealing process (up to 250 °C) as the single crystal. Despite a surface corrugation reaching several hundred picometers (Fig. S6), we were still able to identify regions with stable tunneling junctions and acquire high-resolution STS spectra. As reported previously, the superconducting critical temperature and critical field of Pb depend on sample morphology (nanoscale islands,[42] thin-film thickness, grain size,[43,44] epitaxial substrate[41,45]) and the critical field can be enhanced by up to two orders of magnitude. Our measurements indicate a superconducting-to-normal transition at a sample stage temperature of ~7 K, consistent with Pb(110) single crystal [Fig. 9(c)]. However, its critical field under the tip exceeds ~0.5 T, substantially exceeding the measured value of 0.09 T for the Pb(110) substrate [Fig. 9(d)]. This increased critical field in the foil likely originates from its polycrystalline nature in which grain boundaries can act as effective flux pinning centers.[46]

IV. CONCLUSION

In summary, we have developed a sub-K STM system based on a remote-liquefaction cryogen-free scheme. The system operates in two refrigeration modes: ^{4}He–^{4}He, achieving a base (effective electron) temperature of 894 mK (1.06 K), and ^{4}He–^{3}He, reaching 420 mK (610 mK). In the sub-K regime, temperature stability of approximately ±0.1 mK is maintained via PID control. The system is designed to be compatible with cryogen-free, room-temperature-bore superconducting magnets, as demonstrated here using a 5 T magnet. STM imaging and spectroscopic characterizations demonstrate performance comparable to conventional liquid-helium-based ("wet") systems. The modular remote-liquefaction approach offers key advantages over wet systems: long-term continuous operation, broad temperature tunability, direct high-temperature bake-out capability, straightforward magnet upgradability, and minimal installation space requirements. Moreover, the proposed remote-liquefaction strategy facilitates high-efficiency operations for scanning probe microscopes and serves as an ideal platform for artificial intelligence integration, remote automation, multifield modulation experiments, and complex atomic-scale fabrication. Beyond its current capabilities, this framework can be extended to support dilution refrigerators for measurements under even more extreme conditions.

SUPPLEMENTARY MATERIAL

The supplementary material includes details on the alignment of the dry magnet system integrated with STM, the filtering scheme of the STM system, and the temperature variations at base temperature without proportional–integral–derivative (PID) control. It also provides an analysis of the origin of the obvious peaks in the noise spectrum, along with photographs and STM images of the scraped Pb foil.

ACKNOWLEDGMENTS

The authors are grateful to Professor Hui Guo (IOP, CAS) for the helpful discussion. This work was supported by the National Science Fund for Distinguished Young Scholars (Grant No. T2125014),

the National Key Research and Development Program of China (Grant Nos. 2024YFF0727100, 2025YFF1501200), the Scientific Research Instrument and Equipment Development Project of CAS (Grant Nos. PTYQ2024TD0011, PTYQ2024BJ0005), and the Beijing Natural Science Foundation (Grant No. L245001).

AUTHOR DECLARATIONS

Conflict of Interest

The authors have no conflicts to disclose.

Author Contributions

R.-S. Ma and Y.-Z. Huang contributed equally to this work.

Ruisong Ma: Conceptualization (equal); Data curation (equal); Formal analysis (equal); Funding acquisition (equal); Writing – original draft (lead); Writing – review & editing (equal). **Yuanzhi Huang**: Data curation (equal); Formal analysis (equal); Investigation (equal); Validation (equal); Writing – review & editing (equal). **Guangyuan Han**: Data curation (supporting); Formal analysis (supporting); Writing – review & editing (supporting). **Hao Li**: Methodology (equal); Visualization (equal). **Chenshuai Shi**: Validation (supporting); Visualization (supporting). **Fan Wang**: Methodology (supporting); Validation (supporting). **Xiaodong Yu**: Methodology (supporting); Validation (supporting). **Songping He**: Validation (supporting). **Dairong Liu**: Validation (supporting); Visualization (supporting). **Li Liu**: Software (lead). **Shesong Huang**: Conceptualization (equal); Methodology (equal); Writing – review & editing (supporting). **Hong-Jun Gao**: Project administration (equal); Resources (equal); Writing – review & editing (supporting). **Qing Huan**: Conceptualization (equal); Resources (lead); Supervision (lead); Writing – review & editing (equal).

DATA AVAILABILITY

The data that support the findings of this study are available from the corresponding author upon reasonable request.

REFERENCES

[1]G. Binnig, C. F. Quate, and C. Gerber, Phys. Rev. Lett. **56**(9), 930–933 (1986).
[2]K. Bian, C. Gerber, A. J. Heinrich, D. J. Müller, S. Scheuring, and Y. Jiang, Nat. Rev. Methods Primers **1**(1), 36 (2021).
[3]M. F. Crommie, C. P. Lutz, and D. M. Eigler, Science **262**(5131), 218–220 (1993).
[4]Z.-B. Wu, Z.-Y. Gao, X.-Y. Chen, Y.-Q. Xing, H. Yang, G. Li, R. Ma, A. Wang, J. Yan, C. Shen, S. Du, Q. Huan, and H.-J. Gao, Rev. Sci. Instrum. **89**(11), 113705 (2018).
[5]G. He, Z. Wei, Z. Feng, X. Yu, B. Zhu, L. Liu, K. Jin, J. Yuan, and Q. Huan, Rev. Sci. Instrum. **91**(1), 013904 (2020).
[6]A. M. Coe, G. Li, and E. Y. Andrei, Rev. Sci. Instrum. **95**(8), 083702 (2024).
[7]B. C. Stipe, M. A. Rezaei, and W. Ho, Rev. Sci. Instrum. **70**(1), 137–143 (1999).
[8]R. Ma, H. Li, C. Shi, F. Wang, L. Lei, Y. Huang, Y. Liu, H. Shan, L. Liu, S. Huang, Z.-C. Niu, Q. Huan, and H.-J. Gao, Rev. Sci. Instrum. **94**(9), 093701 (2023).
[9]J. Kasai, T. Koyama, M. Yokota, and K. Iwaya, Rev. Sci. Instrum. **93**(4), 043711 (2022).
[10]S. Zhang, D. Huang, and S. Wu, Rev. Sci. Instrum. **87**(6), 063701 (2016).
[11]S. H. Pan, E. W. Hudson, and J. C. Davis, Rev. Sci. Instrum. **70**(2), 1459–1463 (1999).
[12]C. Salazar, D. Baumann, T. Hänke, M. Scheffler, T. Kühne, M. Kaiser, R. Voigtländer, D. Lindackers, B. Büchner, and C. Hess, Rev. Sci. Instrum. **89**(6), 065104 (2018).
[13]J. Wiebe, A. Wachowiak, F. Meier, D. Haude, T. Foster, M. Morgenstern, and R. Wiesendanger, Rev. Sci. Instrum. **75**(11), 4871–4879 (2004).
[14]H. von Allwörden, K. Ruschmeier, A. Köhler, T. Eelbo, A. Schwarz, and R. Wiesendanger, Rev. Sci. Instrum. **87**(7), 073702 (2016).
[15]L. Zhang, T. Miyamachi, T. Tomanić, R. Dehm, and W. Wulfhekel, Rev. Sci. Instrum. **82**(10), 103702 (2011).
[16]J. Liu, K. Zhao, A. Wang, M. Zhang, J. Wang, Y. Hou, W. Meng, and Q. Lu, Chin. J. Chem. Phys. **38**(6), 855–864 (2025).
[17]M. Liebmann, J. R. Bindel, M. Pezzotta, S. Becker, F. Muckel, T. Johnsen, C. Saunus, C. R. Ast, and M. Morgenstern, Rev. Sci. Instrum. **88**(12), 123707 (2017).
[18]M. Kugler, C. Renner, O. Fischer, V. Mikheev, and G. Batey, Rev. Sci. Instrum. **71**(3), 1475–1478 (2000).
[19]A. Kamlapure, G. Saraswat, S. C. Ganguli, V. Bagwe, P. Raychaudhuri, and S. P. Pai, Rev. Sci. Instrum. **84**(12), 123905 (2013).
[20]S.-Y. Guan, H.-S. Liao, B.-J. Juang, S.-C. Chin, T.-M. Chuang, and C.-S. Chang, Ultramicroscopy **196**, 180–185 (2019).
[21]S. Misra, B. B. Zhou, I. K. Drozdov, J. Seo, L. Urban, A. Gyenis, S. C. J. Kingsley, H. Jones, and A. Yazdani, Rev. Sci. Instrum. **84**(10), 103903 (2013).
[22]Y. J. Song, A. F. Otte, V. Shvarts, Z. Zhao, Y. Kuk, S. R. Blankenship, A. Band, F. M. Hess, and J. A. Stroscio, Rev. Sci. Instrum. **81**(12), 121101 (2010).
[23]M. Assig, M. Etzkorn, A. Enders, W. Stiepany, C. R. Ast, and K. Kern, Rev. Sci. Instrum. **84**(3), 033903 (2013).
[24]D. Wang, L. Kong, P. Fan, H. Chen, S. Zhu, W. Liu, L. Cao, Y. Sun, S. Du, J. Schneeloch, R. Zhong, G. Gu, L. Fu, H. Ding, and H.-J. Gao, Science **362**(6412), 333–335 (2018).
[25]Y. Wang, Y. Chen, H. T. Bui, C. Wolf, M. Haze, C. Mier, J. Kim, D.-J. Choi, C. P. Lutz, Y. Bae, S.-h. Phark, and A. J. Heinrich, Science **382**(6666), 87–92 (2023).
[26]S.-h. Phark, Y. Chen, H. T. Bui, Y. Wang, M. Haze, J. Kim, Y. Bae, A. J. Heinrich, and C. Wolf, ACS Nano **17**(14), 14144–14151 (2023).
[27]S. Qin, J. Kim, Q. Niu, and C.-K. Shih, Science **324**(5932), 1314–1317 (2009).
[28]H. Zhang, H. Chen, Z. Huang, Z.-A. Wang, G. Han, R. Ma, X. Zhu, W. Ning, C. Shen, Q. Huan, and H.-J. Gao, Chin. Phys. Lett. **42**(12), 120708 (2025).
[29]N. Romming, C. Hanneken, M. Menzel, J. E. Bickel, B. Wolter, K. von Bergmann, A. Kubetzka, and R. Wiesendanger, Science **341**(6146), 636–639 (2013).
[30]M. Li, G. Li, L. Cao, X. Zhou, X. Wang, C. Jin, C.-K. Chiu, S. J. Pennycook, Z. Wang, and H.-J. Gao, Nature **606**(7916), 890–895 (2022).
[31]F. D. Natterer, K. Yang, W. Paul, P. Willke, T. Choi, T. Greber, A. J. Heinrich, and C. P. Lutz, Nature **543**(7644), 226–228 (2017).
[32]H. Wang, P. Fan, J. Chen, L. Jiang, H.-J. Gao, J. L. Lado, and K. Yang, Nat. Nanotechnol. **19**(12), 1782–1788 (2024).
[33]P. Wu, Y. Wang, W. Wang, W. Wang, J. Liu, G. Zhou, H. Chen, H. Wang, S. Chen, J. Sun, and F. Liu, Rev. Sci. Instrum. **95**(11), 115101 (2024).
[34]X. Guan, D. M. Wang, Y. J. Xie, J. Fan, and Z. Q. Ji, Rev. Sci. Instrum. **96**(12), 123901 (2025).
[35]H. Huang, M. Shuai, Y. Yang, R. Song, Y. Liao, L. Yin, and J. Shen, Rev. Sci. Instrum. **93**(7), 073703 (2022).
[36]A. Chijioke and J. Lawall, Cryogenics **50**(4), 266–270 (2010).
[37]G. Hörmandinger, Phys. Rev. B **49**(19), 13897–13905 (1994).
[38]G. Li and E. Y. Andrei, Nat. Phys. **3**(9), 623–627 (2007).
[39]T. Machida, Y. Kohsaka, and T. Hanaguri, Rev. Sci. Instrum. **89**(9), 093707 (2018).
[40]S. Nadj-Perge, I. K. Drozdov, J. Li, H. Chen, S. Jeon, J. Seo, A. H. MacDonald, B. A. Bernevig, and A. Yazdani, Science **346**(6209), 602–607 (2014).

[41] W. H. Li, C. C. Yang, F. C. Tsao, and K. C. Lee, Phys. Rev. B **68**(18), 184507 (2003).
[42] S. Rolf-Pissarczyk, J. A. J. Burgess, S. Yan, and S. Loth, Phys. Rev. B **94**(22), 224504 (2016).
[43] Z. Yang, J. V. de Vondel, W. Gillijns, W. Vinckx, V. V. Moshchalkov, and R. Szymczak, Appl. Phys. Lett. **88**(23), 232505 (2006).
[44] E. Rosseel, T. Puig, M. Baert, M. J. Van Bael, V. V. Moshchalkov, and Y. Bruynseraede, Physica C **282–287**, 1567–1568 (1997).
[45] C. C. Yang, F. C. Tsao, S. Y. Wu, W. H. Li, and K. C. Lee, J. Low Temp. Phys. **131**(3/4), 349–352 (2003).
[46] Y. Wang, H.-F. Qin, J.-Y. He, W.-Y. Jiang, Q.-L. Xiao, and J.-Y. Ge, Physica C **614**, 1354357 (2023).